JOURNAL OF GUIDANCE, CONTROL, AND DYNAMICS
Vol. 34, No. 2, March–April 2011

Spectral Decomposition of Orbital Tori

Ralph E. Bordner III* and William E. Wiesel†
Air Force Institute of Technology, Wright-Patterson Air Force Base, Ohio 45433-7320

DOI: 10.2514/1.49574

The Kolmogorov–Arnold–Moser theorem states that lightly perturbed integrable Hamiltonian systems maintain their multiply periodic, toroidal motion in the phase space. The assertion that Earth-orbiting satellites under the influence of the geopotential mimic this behavior is the underlying premise of this work. This paper focuses on applying trajectory-following spectral methods on selected orbits to decompose them into multiperiodic Fourier series, effectively compressing ephemerides for long-term use. The proposed approach focuses on fitting local spectral structures, denoted as frequency clusters, within the sampled orbital data to the analytical form of the windowed, truncated, continuous Fourier transform. This approach is significantly more numerically efficient than fitting every coefficient within the *N*-tuple Fourier series simultaneously. Numerical simulations using integrated data yield root-mean-square error in orbital tori fits at 10 m or less per coordinate axis over a one-year period for most low-inclination, low-eccentricity orbits with altitudes lower than 1900 km.

I. Introduction

IN 1954, Kolmogorov [1] announced a theorem that stated the *N*-dimensional torus (where *N* are the degrees of freedom of the system) whose surface is filled with multiply periodic phase-space motions of an integrable Hamiltonian system does not disappear as a result of a small change in the system Hamiltonian. Multiply periodic is used here to indicate the trajectories of the system experience simple periodic motion in each coordinate, but the frequencies of each axis are not rationally related such that the overall motion is not simply periodic. Because of contributing work by Moser [2] and Arnold [3] in the early 1960s, the theorem is now known as the Kolmogorov–Arnold–Moser (KAM) theorem, in their collective honor. Simply stated, the results of this theorem mean that the multiply periodic motion of such a Hamiltonian system remains multiply periodic under small perturbations and that the resulting motion is just a deformed version of the original motion. Thus, the complicated 2*N* phase-space motion of a nonlinear lightly perturbed system remains highly deterministic. The impact of KAM theory on Earth-orbiting satellites may be an evolutionary upgrade to the most commonly used baseline orbital mechanics solution, since it would replace the current approach of using a solution to the *approximate* orbital motion with what is believed to be an approximate solution to the *actual* motion.

Wiesel [4] first sought to apply trajectory-following spectral methods about the Earth after inspiration from galactic dynamics research by Binney and Spergel [5,6], McGill and Binney [7], and Binney and Kumar [8]. Wiesel [4] shows numerically that invariant tori appear to be prevalent about the Earth and through numerical analysis similar to Laskar's [9,10] numerical analysis of fundamental frequencies (NAFF), he modeled Earth orbits as invariant KAM tori. Following this initial work, Craft [11] focused on orbital formation flight on a torus, and Little [12] attempted to fit KAM tori to the orbits of real-world, Earth-orbiting satellites: the NASA-managed Earth-observation programs of Jason and GRACE (Gravity Recovery and Climate Experiment) [12]. These two efforts used modified NAFF algorithms and both works were plagued by local Fourier transform effects, primarily attributable to the use of small, finite time data batches. Although both efforts could benefit from further refinement of their initial torus estimates by a fitting algorithm like least-squares, this would involve inversion of square matrices whose size is on the order of the number of coefficients desired. In addition to their large size, these matrices are often poorly conditioned. This paper proposes a new way to efficiently and more precisely spectrally decompose an orbital trajectory by using the analytical form of the windowed, truncated, continuous Fourier transform such that the presumed underlying orbital torus is better revealed.

Received 28 May 2010; revision received 30 September 2010; accepted for publication 1 October 2010.

*Major, USAF; Deputy Chief, Layered Sensing Exploitation Division; U.S. Air Force Research Laboratory, Building 620, 2241 Avionics Circle. Senior Member AIAA.

†Professor, Astronautical Engineering, Department of Aeronautics and Astronautics, 2950 Hobson Way. Member AIAA.

II. Theoretical Preliminaries

Pure analytical approaches to find KAM tori usually require significant constraints on the system under consideration, especially if an *n*-body system is being analyzed. Further, current analytical methods find it difficult to obtain closed-form solutions for any problems of significant practical concern due to large perturbations, including those about the Earth. As such, this research presents a numerically based method to construct a KAM torus about the Earth. Before detailing the proposed numerical techniques and procedures, a brief discussion on the underlying mathematical theory is warranted to motivate the numerical work as well as to provide a foundation from which to build it.

A. Unperturbed Motion

Integrable, periodic Hamiltonian systems are multiply periodic. Recall that multiply periodic motion is defined here as being composed of periodic motion with *N* fundamental frequencies, Ω_j, thus it can be modeled as an *N*-tuple Fourier series of the form

$$\mathbf{q}(t) = C_{(0,0,\ldots,0)^N} + \sum_{\mathbf{j}} \{C_{\mathbf{j}} \cos(\mathbf{j} \cdot \mathbf{\Omega} t) + S_{\mathbf{j}} \sin(\mathbf{j} \cdot \mathbf{\Omega} t)\} \quad (1)$$

where *C* and *S* are the Fourier coefficients, $\mathbf{\Omega}^T = (\Omega_1, \Omega_2, \ldots, \Omega_N)$ is the basis-frequency set, *N* is the dimension of the basis set, $\mathbf{q}(t)$ is the time history of the reconstructed sampled position data, and the multiple-index summation vector $\mathbf{j}^T = (j_1, j_2, \ldots, j_N)$ is expanded out to any arbitrary integer limit in each element according to the vector

$$\mathbf{M} = (\text{index limit}_{j_1}, \text{index limit}_{j_2}, \ldots, \text{index limit}_{j_N}) \quad (2)$$

The summation vector $\mathbf{j}$ must be chosen with care as to avoid symmetrical trigonometric properties [i.e., $\cos(x) = \cos(-x)$]. The end Fourier series representation will be a set of *M*-order Fourier series coefficients in each coordinate axis and one full set of *N* independent frequencies (i.e., common to all axes). From an

equations-of-motion perspective, the multiply periodic motion can be described in terms of the apparently ironically named constant *action I* and linearly varying *angle* θ variables:

$$\dot{I}_j = 0 \tag{3}$$

$$\dot{\theta}_j = \frac{\partial \mathcal{H}(I)}{\partial I_j} = \Omega_j(I) \tag{4}$$

In this case, the phase-space motion is restricted to lie on the surface of an N-dimensional torus, also referred to as an N-torus. If the fundamental frequencies are incommensurate, then the motion of the system will densely fill the surface of a nonresonant torus. Otherwise, the motion will lie on a resonant torus and the system trajectories will close upon each other. This toroidal behavior of an integrable Hamiltonian system is given by the Liouville–Arnold theorem.

B. Perturbed Motion

It is a common hypothesis that many systems can be modeled as a lightly perturbed, integrable system, and this hypothesis is the underlying assumption of this work. In fact, this paper is simply a numerical search for, and subsequent exploitation of, orbital motion that mimics the known solutions of a system whose Hamiltonian function $\mathcal{H}$ is that of an integrable Hamiltonian function $\mathcal{H}_o$ plus that of small perturbation, $\mathcal{H}_1$. If we assume the standard perturbation theory terminology, we can state this mathematically as

$$\mathcal{H}(\mathbf{I}, \theta) = \mathcal{H}_o(\mathbf{I}) + \epsilon \mathcal{H}_1(\mathbf{I}, \theta) \tag{5}$$

where ϵ is a small, real perturbation parameter much less than 1, and $\mathcal{H}_o$ and $\mathcal{H}_1$ are real analytic functions. The solution to this problem perplexed many for years and Poincaré called it the fundamental problem of dynamics. As introduced previously, Kolmogorov [1] conjectured with an outline of a proof, as follows:

Theorem 1: If an unperturbed system is nondegenerate, then for sufficiently small conservative Hamiltonian perturbations, most nonresonant invariant tori do not vanish, but are only slightly deformed, so that in the phase space of the perturbed system, too, there are invariant tori densely filled with phase-space curves winding around them conditionally periodically, with a number of independent frequencies equal to the number of degrees of freedom. These invariant tori form a majority in the sense that the measure of the complement of their union is small when the perturbation is small [3].

Essentially, the KAM theorem takes the perturbed Hamiltonian in Eq. (5), assumes an N-dimensional tori exists, and then seeks out an action-angle coordinate transformation to map the perturbed Hamiltonian to that of a new one such that it is a function of the new action variables only:

$$\mathcal{H}(\mathbf{I}, \theta) = \mathcal{H}'(\mathbf{I}') \tag{6}$$

The new Hamiltonian, $\mathcal{H}'$, is found by solving the Hamilton–Jacobi equation for the generating function S:

$$\mathcal{H}'(\mathbf{I}') = \mathcal{H}\left(\frac{\partial S(I', \theta)}{\partial \theta}, \theta\right) \tag{7}$$

Once found, the transformation to switch between old and new coordinates/momenta is accomplished via standard techniques. The initial proofs of Kolmogorov's theorem were to solve the Hamilton–Jacobi equation in Eq. (7) through *superconvergent*, iterative methods similar to Newton's method, thereby circumventing the problem of small divisors [13]. The rapid convergence is possible via this type of approach, since the series is approximated at each step using the best estimate available rather than with what the series initially used. The KAM theorem shows that solutions converge quickly when the perturbations are *sufficiently small* and the N frequencies are *sufficiently incommensurate*, thereby showing perpetual stability for the system. To guarantee sufficient incommensurability, the independent frequencies are usually held to diophantine condition from number theory:

$$\left|\sum_{i=1}^{N} a_i \omega_i\right| \geq C\|a\|^{-\nu} \quad \text{for all } a = \{a_1, a_2, \ldots, a_n\} \in \mathbb{Z}^n \tag{8}$$

where $C \geq 0$ and $\nu \geq 0$. From the perspective of Lebesgue measure, the survival of invariant tori is found to happen *most* of the time, and as ϵ goes to zero, so does the size of the phase-space volume not containing invariant tori. For those resonant tori whose frequencies are approximated by rationals, they find themselves destroyed after a perturbation and they are often replaced by pairs of hyperbolic and elliptic orbits in the vacated phase space. These orbits are accompanied commonly by chaotic orbits as well [14].

C. KAM Tori Existence About the Earth

For n-body problems, especially those within our solar system and about the Earth, analytic solutions have been elusive due to the prohibitive size of the perturbation parameter. However, recent efforts using computer-assisted proofs have produced good results in a few cases within the solar system [15]. Because of these difficulties, a justifiable question to ask might be, "Do invariant KAM tori really exist about the Earth?" A first response to this question is that although it is sufficient for perturbations to be small for tori to exist, the KAM theorem does not state that it is necessary. Secondly, based on numerical research by Wiesel [4], it appears that invariant KAM tori do generally exist about the Earth, or at least almost invariant ones. This latter statement appears to be supported by work by Deshalms and Gutiérrez [16] with Nekhoroshev's theorem [17], which pertains to a system's relative stability as opposed to the absolute stability described by KAM theory. According to their proof of Nekhoroshev's theorem, it may be possible to find Earth-orbiting trajectories that essentially appear to reside on KAM tori and will remain so on timescales sufficiently long enough for satellite applications. They define these apparent tori as nearly invariant tori.

III. Orbital Tori Spectra

As posited by Wiesel [4], there are three basis frequencies for the geopotential-only solution to the Earth-orbiting problem. Each of these frequencies have clear physical interpretations within the Earth-fixed frame. The first frequency, the anomalistic frequency, is nearly the mean motion of the orbit itself. It is approximately the resulting mean motion due to the secular effects of the geopotential considering only J_2. Thus, this frequency can crudely be described as "setting up" the satellite's orbit as it describes the dominant rotational motion about the Earth. This frequency is approximately

$$\Omega_{1,J2} \approx \sqrt{\frac{\mu}{a^3}}\left\{1 - \frac{3J_2R_\oplus^2}{2a^2(1-e^2)^{\frac{3}{2}}}\left(\frac{3}{2}\sin^2 i - 1\right)\right\} \tag{9}$$

The next frequency corresponds to the previously established orbital motion precessing in the Earth's rotating frame due to J_2, hence it is a combination of the Earth's rotational frequency and the nodal regression rate. This frequency is estimated to be

$$\Omega_{2,J2} \approx \omega_\oplus + \frac{3\sqrt{\mu}J_2R_\oplus^2}{2a^{\frac{7}{2}}(1-e^2)^2}\cos i \tag{10}$$

Finally, the last of the basis frequencies was determined to be the description of the motion introduced into the problem by the geopotential should the orbit not be perfectly circular. As such, it describes the rotation of the line of apsides, or the apsidal regression rate. This frequency is estimated to be

$$\Omega_{3,J2} \approx -\frac{3\sqrt{\mu}J_2R_\oplus^2}{2a^{\frac{7}{2}}(1-e^2)^2}\left(\frac{5}{2}\sin^2 i - 2\right) \tag{11}$$

In each of these expressions, $R_\oplus$ is the radius of the Earth, μ is the Earth's gravitational parameter, J_2 is the zonal harmonic coefficient of the Earth's geopotential due to the oblateness of the Earth, $\omega_\oplus$ is the Earth's rotation frequency, e is the orbital eccentricity, a is the orbital semimajor axis, and i is the orbital inclination. In hindsight,

the basis set is composed of frequencies that are already known from analysis of linearized perturbations about the Earth [18], but under the paradigm of KAM theory they have taken on a new, geometrical meaning: the rotational frequencies about a six-dimensional torus.

The three basis frequencies manifest in a repetitive and organized fashion within the spectral plot of the orbital data. A notional representation of a small section of a typical orbital torus' Fourier transform is seen in Fig. 1. The larger, central spectral lines form a common pattern within the transform plot, a triplet structure. If the torus is the fully degenerate case of the two-body problem, the spectral lines would be one copy of this triplet structure (i.e., only the larger, central lines). In this instance, the middle line would be exactly the mean motion and the flanking lines would be the mean motion $\pm$ the rotation rate of the Earth.

The simple triplet pattern of the two-body problem takes on a much richer detailed look when under the influence of the full geopotential (or high-order geopotential model for integrated data). In this case, this triple-line formation (to include the surrounding smaller spectral lines) is copied over and over again in an asymptotically decreasing fashion along the frequency axis, although this is an oversimplified explanation. In reality, the spectra are an ever-decreasing set of spectral lines corresponding to harmonics of every integer combination of the basis-frequency set. In fact, the frequencies that compose the triplet structure while under the influence of the full geopotential are integer multiples of the entire basis set as opposed to just the mean motion and the Earth's rotational frequency. Table 1 decomposes the main triplet into its individual basis-frequency components under this scenario. For this example, the peaks in the main triplet structure have been numbered 1 through 3, from left to right. Regardless, the smaller spectral lines surrounding each of the larger, central lines within the plot in Fig. 1 are a crude representation of this detail. These flanking peaks are decaying echoes of the smallest basis frequency, which is approximately $\Omega_{3,J2}$. Although all three spectral lines of the triplet are found in each axis, the centerline is most prominent in the Z axis, whereas the other two are strongest in the X and Y axes. This is due to the chosen rotating reference frame.

IV. Trajectory-Following Spectral Decomposition

Trajectory-following methods are any methods that seek to find tori from a vector of sequential positional data as opposed to the equations of motion themselves. The benefits of spectral methods are that they appear to find tori where analytical methods have difficulty; however, they require long samples of orbital trajectories and time-consuming numerical methods. Wiesel [4], Little [12], and Craft [11] all found considerable success using trajectory-following methods. Although the details of their methods may differ, the core of their approaches, as well as the one in this paper, are similar.

A. General Approach

Under the key assumptions that orbital motion is truly multiply periodic and that the nondegeneracy and diophantine conditions from KAM theory are met, the overall goal is to find an N-tuple Fourier series representation of the orbital torus, as introduced in Eq. (1). The general approach to find the missing Fourier parameters in this expression is almost intuitively obvious. First, a highly accurate approximation of the basis frequencies must be made. Second, the Fourier series coefficients (i.e., the amplitude of the Fourier transform at each integer combination of the basis frequencies) must be determined. These coefficients are found directly from analysis of the Fourier transform of the data according to the following:

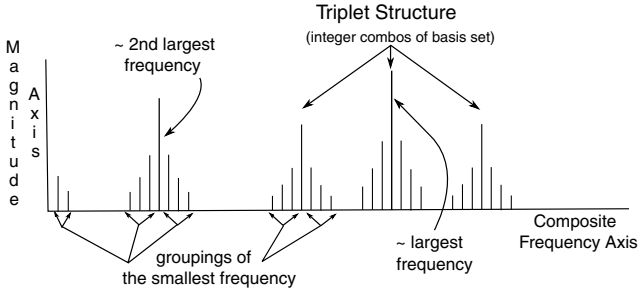

Fig. 1 Notional depiction of orbital torus spectra.

Table 1 Spectral decomposition of main triplet

Triplet line	$\lvert\Omega_1\rvert$	$\lvert\Omega_2\rvert$	$\lvert\Omega_3\rvert$
1	1	−1	−1
2	1	0	−1
3	1	1	−1

$$C_{(\mathbf{0},\mathbf{0},\ldots,\mathbf{0})^N} = \Re\Phi(0) \tag{12}$$

$$C_{\mathbf{j}} = 2\Re\Phi(\Psi_{\mathbf{j}}), \quad \text{and} \tag{13}$$

$$S_{\mathbf{j}} = -2\Im\Phi(\Psi_{\mathbf{j}}) \tag{14}$$

where $\Re$ and $\Im$ are the real and imaginary portions, respectively, of the Fourier transform Φ. Here, $\Phi(\Psi_{\mathbf{j}})$ is defined as the Fourier transform of the data at $\Psi_{\mathbf{j}}$, where $\Psi = (k_1\Omega_1 + k_2\Omega_2 + \cdots + k_m\Omega_m)$, for $k \in \mathbb{Z}$, and in accordance to the summation vector $\mathbf{j}$. Thus, Ψ is a composite coordinate variable composed of integer multiples of the basis set representing each spectral line. At this point, all unknowns would be resolved and an initial torus could be constructed. The quality in the fit of this torus could be made by calculating the error in the fit by differencing the reconstructed orbital data with the original data set. For precision applications, the error in the fit would need to be on the order of meters over the given time span.

B. NAFF-Based Fourier Analysis Methods

Laskar's [9,10] NAFF approximates the truncated, continuous Fourier transform of a function, $\mathbf{f}(t)$, by scalar product, as opposed to using faster DFT methods, in order to minimize the effects of aliasing and leakage within the Nyquist interval [19]. When using a Hanning window of order one [9], the NAFF has been shown to converge upon the fundamental frequencies at a rate of $1/T^4$ for KAM problems instead of $\frac{1}{T}$ by standard Fourier transform methods, where T is half the sample interval. To estimate the fundamental frequencies for the multiply periodic approximation and every integer combination thereof at frequencies above zero, the NAFF finds the maximum amplitude of

$$\phi(\omega) = \langle \mathbf{f}(t), e^{-i\omega t)} \rangle \tag{15}$$

where the scalar product $\langle \mathbf{f}(t), \mathbf{g}(t) \rangle$ is defined by

$$\langle \mathbf{f}(t), \mathbf{g}(t) \rangle = \frac{1}{2T} \int_{-T}^{T} \mathbf{f}(t)\bar{\mathbf{g}}(t)\chi\left(\frac{t}{T}\right) \mathrm{d}t \tag{16}$$

and where $\chi(t)$ is a weight function that is a positive even function, such that

$$\frac{1}{2} \int_{-1}^{1} \chi(t)\, \mathrm{d}t = 1 \tag{17}$$

Laskar [9,10] uses a Hanning window of the form

$$\chi_p\left(\frac{t}{T}\right) = \frac{2^p(p!)^2}{(2p)!}\left(1 + \cos\left(\pi\frac{t}{T}\right)\right)^p \tag{18}$$

where p is the order of the Hanning window function. This paper uses the NAFF to establish frequency estimates at prominent spectral lines in each axis and then subsequently uses those approximations in a least-squares solution for a final estimate of the basis set. Once a basis set is established, a NAFF-based decomposition method can approximate the orbital torus by decomposing the Fourier transform

according to the N-tuple Fourier series by orderly approximating and storing the Fourier coefficients at every integer combination of the basis set desired.

Laskar's [9] first NAFF paper postulated its assertions based on a Hanning window of order 1. However, he does show in a subsequent paper [10] that the order of the window, p, can take on integer values between 1 and 5, depending on the level of accuracy needed and the regularity of the motion. For $p > 5$, gains in convergence are greatly diminished. For this work, a Hanning window of $p = 2$ was used primarily. This is due to the fact that as p increases, so does the width of the main lobe. Although this assists in frequency resolution and side-lobe suppression, it does increase the opportunity of the main lobe occluding any nearby peaks. This was also noticed by Wiesel [4] and Little [12] as well as commented on by Gomez et al. [20].

Clearly, the NAFF is similar to common Fourier analysis methods. Of course, instead of the familiar Fourier integral, the Fourier transform was calculated as a scalar product between the vectors of weighted sampled data values and $e^{-i\omega t}$, with the desired number of frequency points ω, depending on the level of frequency granularity desired in the transform output. Generally speaking, this research found it beneficial to use a large number of frequency points, especially when investigating a data set for the first time. Too few points may obscure fine details in the spectral content, such as the cascading harmonics of the apsidal regression frequency about the two faster frequencies in the basis set. The strength in the NAFF algorithm lies in the fact that aliasing and leakage are thoroughly mitigated and that it converges much more quickly than standard methods. The penalties are time-consuming numerical evaluations and the potential to introduce errors during the approximation of the numerical integrals. The numerical integrals approximated in this paper were done via simple quadrature methods (specifically, 3/8 and/or 1/3 Simpson's rules), depending on the number of data samples to analyze. Regardless, the keys in implementing the NAFF algorithm are to sample fast enough to avoid aliasing effects, long enough to mitigate leakage, and to apply a window function of appropriate characteristics such that leakage is further minimized without affecting nearby frequency identification.

V. Proposed Method

Laskar [9,10] used the NAFF with millions of years of integrated data. As such, the spectral plots could be expected to be dominated by sharp peaks. Although they may not have been true Dirac delta functions, which would be attained with an infinite data sample, they most certainly were much closer to these ideal representations than what can be attained with only weeks to a few years of Earth-orbiting satellite data. Because of this, Laskar did not experience significant problems manifesting from interfering lobe shoulders and wide main lobes. However, the work of Wiesel [4], Craft [11], and Little [12] was forced to endure these effects, all of which threaten to undermine the quality of the orbital torus estimate. Although longer and more frequent sampling may provide some relief from these issues, they will not fully eliminate them. It was believed that the way to properly account for these short-data-window artifacts was to use the windowed analytical form of the truncated, continuous, Fourier transform (ATCFT) in the fitting process as opposed to determining the Fourier coefficients directly from the spectral plot. The method proposed in this paper using the ATCFT was implemented with considerable benefit. It bases its approach on sectioning the spectral plot into groups of frequency lines, instead of a collection of individual peaks, and using the ATCFT to fit them. These structures are denoted here as frequency clusters. In addition to mitigating undesired transform effects, the frequency-cluster approach is also much more numerically efficient and sound than trying to globally fit all spectral lines simultaneously. For example, Gomez et al. [20] have developed a three-step numerical procedure for the Fourier analysis of quasi-periodic functions using the discrete Fourier transform (DFT). The method first requires estimates of the frequencies of interest, N_f, to be estimated. Then using these frequencies and leveraging the fact that the DFT approximation of the quasi-periodic motion is linear, initial estimates of the corresponding amplitudes are found by solving a $(1 + 2N_f \times 1 + 2N_f)$ linear system. Finally, the estimates of the amplitudes and frequencies are refined by solving a larger system of equations, consisting of the previously described linear system plus an additional nonlinear equation for each system frequency, using Newton's method. The method presented in this paper only requires two steps and trades solving one very large linear system of equations with a sequence of much smaller linear systems. In addition to not having to solve a second set of equations, there is a large savings in computational effort by solving dozens of small systems, instead of one massive linear system.

A. Frequency-Cluster-Based Approach

In addition to reducing computational burden, employing the ATCFT in the fitting process mitigates some problems associated with short-length data samples, since the exact shape of the Fourier transform is taken into account. By using the ATCFT, a decomposition algorithm is allowed to successively solve for and extract local bands of coefficients and their associated frequency content under local transform effect (i.e., effects from large main lobes as well as shoulders of nearby transform peaks). To further motivate this concept, a plot of the high-resolution Fourier transform from an integrated orbit is shown in Fig. 2, where the X, Y, and Z axes are shown from top to bottom, respectively. The orbit portrayed is a low Earth orbit (LEO) with an approximate semimajor axis of 1.1 Earth radii $R_\oplus$, an eccentricity of 0.05, and an inclination of 30 deg. A closer inspection of the main triplet in the Z axis in Fig. 3 reveals the rich Ω_3 detail hinted at in Fig. 2. Figure 3 also shows the most significant local aberrations in the transform more clearly and reveals that in addition to the shoulders and peak widths within a cluster affecting coefficient determination, the shoulders from nearby clusters are also troublesome. Although the former is mitigated by the ATCFT, the latter can be addressed by extracting each frequency cluster's contribution to the data in descending order of magnitude.

B. Orbit Survey

Because of the usually long-period motion, relatively speaking, of the smallest basis frequency, which corresponds to the apsidal regression rate, trajectory-following methods usually have difficulties converging on it with sufficient precision. Treating it as static is not permissible, since it does not simply manifest as itself, but also as part of faster, more dominant frequencies within the data. A survey of how Ω_3 changes with semimajor axis, eccentricity, and inclination was accomplished to see which orbits may allow the most success for trajectory-following methods. The plots in Figs. 4 and 5 show graphical forms of some results due to a particular set of initial conditions. The plot in Fig. 4 shows estimates of Ω_3 due to J_2, varying on the orbital parameters of inclination and semimajor axis.

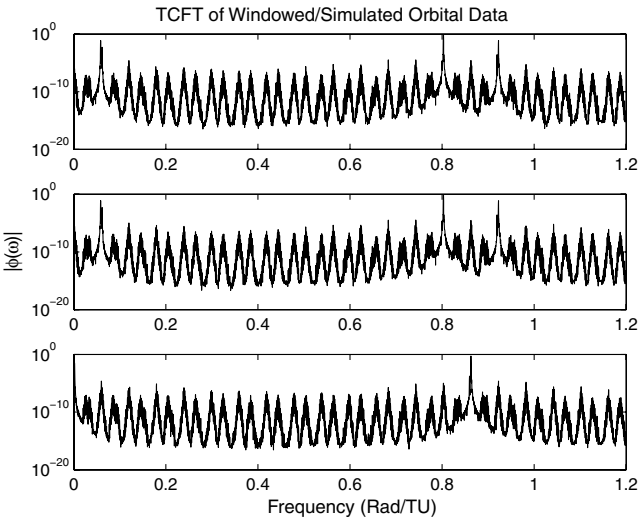

Fig. 2 Spectra of integrated orbit ($a = 1.1R_\oplus$, $e = 0.05$, and $i = 30$ deg).

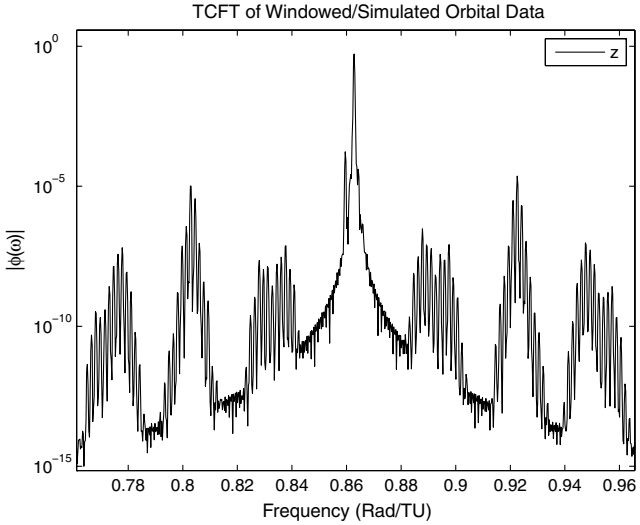

Fig. 3 High-detail plot of integrated orbit's primary triplet.

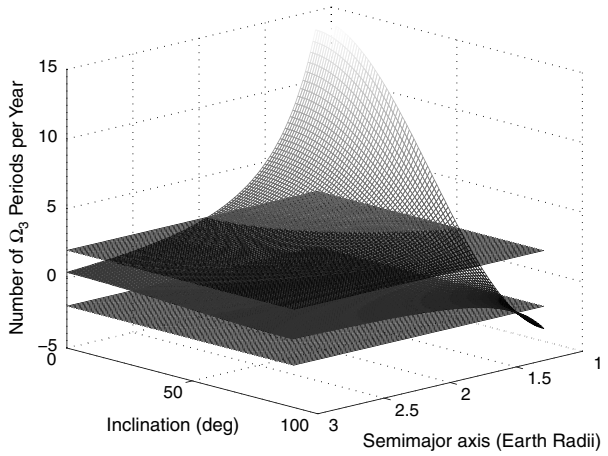

Fig. 4 Sweep on inclination/semimajor axis.

The plot assumes a static value of 0.01 for eccentricity and that only one year of data is available. The two horizontal axes are intuitive, but the vertical axis shows the number of periods of Ω_3 in a one-year interval instead of using the more expected form of frequency units. This was done to more clearly convey where the useful limits within the data lie. Because of sampling restrictions similar to those of the Nyquist–Shannon sampling theorem, approximately two periods of Ω_3 are needed within a data set to sufficiently capture it spectrally in the Fourier transform. Hence, planes are inserted at ± 2 periods per year. The sign of the frequency represents direction of rotation and not a positive or negative frequency. Clearly, from this picture, Ω_3 quickly approaches the no-go limit as the semimajor axis approaches two Earth radii and/or the inclination nears the critical inclination. Although the plane limits are clear stops, practical limits lie somewhere short of them, depending on the level of precision required of the orbital torus estimate. The plot in Fig. 5 has been included here to illustrate that a change in eccentricity has a much smaller effect on Ω_3 than does inclination and semimajor axis. In this plot, the semimajor axis is held constant at 1.1 $R_\oplus$, and inclination and eccentricity are varied.

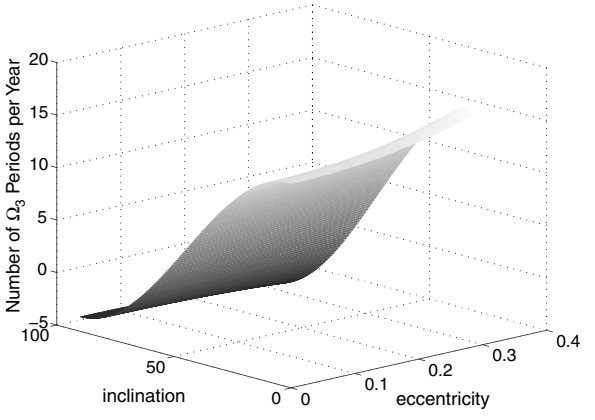

Fig. 5 Sweep on inclination/eccentricity.

C. Geopotential Model and Satellite Dynamics

The geopotential model $\mathcal{V}$ chosen for the numerical integrator within this work was a spherical harmonic model with coefficients through the 21st order and degree [21]. The coefficients used were taken from the NASA EGM96 solution.[‡] This model was placed in a frame that is stationary with respect to the geopotential and tied to the center of and rotating with the Earth. This frame is modeled as a simple, Cartesian coordinate system whose X-Z plane is formed by orthogonal rays originating from the center of the Earth and passing through the Prime Meridian and North Pole, respectively. The Y axis lies in the plane of the equator with the X axis and is found as the right-hand rule is completed. The difference between it and the Earth-centered inertial frame is a single rotation about the Z axis through an angle formed between the inertial reference point and the Prime Meridian. Choosing a satellite's rectangular coordinate vector $\mathbf{r}$ in the Earth-centered, Earth-fixed (ECEF) frame as the generalized coordinate position vector $\mathbf{q}$, the time derivatives of this vector simply become the inertial velocities resolved in the ECEF frame:

$$\dot{\mathbf{r}} = \mathbf{v} = \begin{bmatrix} \dot{x} - \omega_\oplus y \\ \dot{y} + \omega_\oplus x \\ \dot{z} \end{bmatrix} \tag{19}$$

where $\omega_\oplus$ is the rotation rate of the Earth. The kinetic energy is easily calculated as $\mathcal{T} = \frac{1}{2}\mathbf{v}^2$ such that the Lagrangian $\mathcal{L}$ becomes

$$\mathcal{L} = \mathcal{T} - \mathcal{V} = \frac{1}{2}((\dot{x} - \omega_\oplus y)^2 + (\dot{y} + \omega_\oplus x)^2 + (\dot{z})^2) - \frac{\mu}{r}\sum_{n=1}^{\infty}\sum_{m=1}^{n}\left(\frac{r}{R_\oplus}\right)^{-n} P_n^m[\sin(\delta)]\{C_{nm}\cos(m\lambda) + S_{nm}\sin(m\lambda)\} \tag{20}$$

where μ is the gravitational parameter; $R_\oplus$ is the equatorial radius of the Earth; C_{nm} and S_{nm} are the field coefficients that complete the gravity model; and P_m^n are the usual associated Legendre polynomials. The radius r, geocentric latitude δ, and east longitude λ, are found from

$$r = \sqrt{x^2 + y^2 + z^2} \tag{21}$$

$$\sin(\delta) = \frac{z}{\sqrt{x^2 + y^2}} \tag{22}$$

$$\tan(\delta) = \frac{y}{x} \tag{23}$$

Thus, the momenta become the following after applying $p_i = \partial\mathcal{L}/\partial\dot{q}_i$:

$$\mathbf{p} = \begin{bmatrix} \dot{x} - \omega_\oplus y \\ \dot{y} + \omega_\oplus x \\ \dot{z} \end{bmatrix} \tag{24}$$

which are just the inertial velocities resolved in the rotating Earth frame that were found previously. Inverting the momenta to form the coordinate velocities $\dot{q}_i$ in terms of the momenta, forming the Hamiltonian according to

[‡]Data available online at http://cddis.nasa.gov/926/egm96/egm96.html [retrieved November 2010].

$$\mathcal{H} = \sum_i p_i \dot{q}_i - \mathcal{L}$$

and applying Hamilton's equations gives the equations of motion as

$$\begin{bmatrix} \dot{\mathbf{q}} \\ \dot{\mathbf{p}} \end{bmatrix} = \begin{bmatrix} p_x + \omega_\oplus q_y \\ p_y - \omega_\oplus q_x \\ p_z \\ \omega_\oplus p_y - \frac{\partial \mathcal{V}}{\partial q_x} \\ \omega_\oplus p_x - \frac{\partial \mathcal{V}}{\partial q_y} \\ -\frac{\partial \mathcal{V}}{\partial q_z} \end{bmatrix} \tag{25}$$

where the partial of the potential function with respect to each coordinate is dependent on the position of the satellite. These equations were integrated with a Hamming fourth-order predictor–corrector algorithm. Since the Hamiltonian is independent in time, it is a constant of the motion. Consequently, it was used as a numerical check of the integrator. For LEO orbits, error in the Hamiltonian was on the order of 10×10^{-13} during a one-year time span.

D. Decomposition by Frequency Clusters

The underlying premise of the frequency-cluster decomposition method is to use the windowed form of the ATCFT to solve for the Fourier coefficients of a set of spectral lines that have strong spectral correlation by setting the analytical approximation of the Fourier transform of each spectral line equal to that of its numerically calculated value. Of note is that the analytical expression used approximates the windowed ATCFT of the cluster by using a summed total of the individual analytical contributions of each frequency line within the cluster. This is noteworthy as it lends itself easily to a system of linear equations. By solving for the imaginary and real portions of the Fourier transform separately, a linear system of n equations and n unknowns materializes, where n is twice the number of frequency lines being fit. Since there are two Fourier coefficients for every line, this gives a square system to solve in the familiar form of

$$A\mathbf{x} = \mathbf{b} \tag{26}$$

The solution vector $\mathbf{x}$ is an $(n \times 1)$ column vector of the alternating sine and cosine Fourier coefficients for each cluster spectral line. The result vector $\mathbf{b}$ is an $(n \times 1)$ column vector of alternating real and imaginary portions of the actual numerically calculated Fourier transform corresponding to the coefficient pairs in the to-be-determined solution vector. The matrix of coefficients A is appropriately composed of coefficients in the linear system. Its construction is somewhat more complicated and requires extra care in its description.

The coefficients of the A matrix in Eq. (26) are alternating rows of the real and imaginary portions of the summed Fourier coefficient terms in the windowed ATCFT expression, with the type of row, depending on the type of value in the result vector (i.e., real or imaginary portion of the calculated Fourier transform value at that frequency line). The nonwindowed ATCFT is obtained by taking the Fourier transform of the presumed N-tuple Fourier series in Eq. (1). After taking the transform, the ATCFT is seen to be

$$\begin{aligned} \text{ATCFT} = C_{(0,0,\ldots,0)^N} \operatorname{sinc}(\omega T) + \sum_{\mathbf{j}} \Bigg\{ & \frac{C_{\mathbf{j}}}{2} \{\operatorname{sinc}((\Psi_{\mathbf{j}} - \omega)T) \\ & + \operatorname{sinc}((\Psi_{\mathbf{j}} + \omega)T)\} + \frac{iS_{\mathbf{j}}}{2} \{\operatorname{sinc}((\Psi_{\mathbf{j}} + \omega)T) \\ & - \operatorname{sinc}((\Psi_{\mathbf{j}} - \omega)T)\} \Bigg\} \end{aligned} \tag{27}$$

where $\Psi_{\mathbf{j}}$ is once again an integer multiple of the basis frequencies according to the summation vector $\mathbf{j}$ and the sinc function is defined as $\operatorname{sinc}(x) = \sin(x)/x$. To get the windowed form of the ATCFT, the desired window function of the form

$$\chi_p\left(\frac{t}{T}\right) = \frac{2^p (p!)^2}{(2p)!} \left(1 + \cos\left(\pi \frac{t}{T}\right)\right)^p \tag{28}$$

where p is the order of the window, must be multiplied with the N-tuple Fourier series form before taking the transform, or the transformed form of the window must be convolved with the version of the ATCFT found in Eq. (27). Either way, this is a daunting task by hand. However, with the aid of Mathematica, the analytical forms of these coefficients were easily obtained. For a Hanning window of order two, the matrix of coefficient's elements for spectral lines within a single frequency cluster are

$$\begin{aligned} \mathcal{C} = & -(2e^{-iT\omega}\pi^4((-1 + e^{2iT\omega})(4i\pi^4\omega - 5i\pi^2T^2\omega(3\Psi^2 + \omega^2) \\ & + iT^4\omega(5\Psi^4 + 10\Psi^2\omega^2 + \omega^4)\cos[T\Psi] \\ & + (1 + e^{2iT\omega})\Psi(4\pi^4 - 5\pi^2T^2(\Psi^2 + 3\omega^2) \\ & + T^4(\Psi^4 + 10\Psi^2\omega^2 + 5\omega^4))\sin[T\Psi]))) / (T(-\Psi^2 + \omega^2) \\ & \times (16\pi^8 + T^8(\Psi^2 - \omega^2)^4 - 40\pi^6T^2(\Psi^2 + \omega^2) - 10\pi^2T^6(\Psi^2 - \omega^2)^2 \\ & \times (\Psi^2 + \omega^2) + \pi^4T^4(33\Psi^4 - 2\Psi^2\omega^2 + 33\omega^4))) \end{aligned} \tag{29}$$

and

$$\begin{aligned} \mathcal{S} = & -(2e^{-iT\omega}\pi^4((-1 + e^{2iT\omega})(4\pi^4\Psi - 5\pi^2T^2(\Psi^3 + 3\Psi\omega^2) \\ & + T^4(\Psi^5 + 10\Psi^3\omega^2 + 5\Psi\omega^4)\cos[T\Psi] - i(1 + e^{2iT\omega})\omega \\ & \times (4\pi^4 - 5\pi^2T^2(3\Psi^2 + \omega^2) + T^4(5\Psi^4 + 10\Psi^2\omega^2 + \omega^4)) \\ & \times \sin[T\Psi]))) / (T(-\Psi^2 + \omega^2)(16\pi^8 + T^8(\Psi^2 - \omega^2)^4 \\ & - 40\pi^6T^2(\Psi^2 + \omega^2) - 10\pi^2T^6(\Psi^2 - \omega^2)^2(\Psi^2 + \omega^2) \\ & + \pi^4T^4(33\Psi^4 - 2\Psi^2\omega^2 + 33\omega^4))) \end{aligned} \tag{30}$$

where $\mathcal{C}$ is the coefficient of each cosine term, $\mathcal{S}$ is the coefficient of each sine term, T is the half-interval of the data, Ψ is the spectral cluster line of interest, and ω is the sweep frequency, which is an element of the vector of frequency-cluster spectral lines currently under investigation. To ease issues with the singularity experienced as Ψ approaches ω, L'Hopital's rule was applied. In this case, the coefficients found previously become

$$\mathcal{C} = \frac{\pi^8\Psi - 5\pi^6\Psi^3 + 4\pi^4\Psi^5 + \pi^8\cos[\Psi]\sin[\Psi]}{2\pi^4\Psi(\pi^4 - 5\pi^2\Psi^2 + 4\Psi^4)} \tag{31}$$

and

$$\mathcal{S} = -\frac{i(\pi^8\Psi - 5\pi^6\Psi^3 + 4\pi^4\Psi^5 - \pi^8\cos[\Psi]\sin[\Psi])}{2\pi^4\Psi(\pi^4 - 5\pi^2\Psi^2 + 4\Psi^4)} \tag{32}$$

In the interest of compactness of the final form of the linear system described in Eq. (26), define the Fourier coefficient pair for each spectral line as $\mathcal{K}$. This makes the (2×1) coefficient row vector for the ith spectral line Ψ_i become $\mathcal{K}_{[\Psi_i]}$ or

$$\mathcal{K}_{[\Psi_i]} = [\,\mathcal{C}_{[\Psi_i]} \quad \mathcal{S}_{[\Psi_i]}\,] \tag{33}$$

where Ψ_i is as before. Thus, the two (2×1) row vectors representing the real and imaginary halves of this coefficient vector $\mathcal{K}_{[\Psi_i]}$ can be written as $\Re(\mathcal{K}_{[\Psi_i]})$ and $\Im(\mathcal{K}_{[\Psi_i]})$, respectively. By labeling each cluster line's Fourier coefficient set with respect to the sweep variable values [i.e., the other spectral lines (Ψ_l: $l = 1, \ldots, n; l \neq i$) in the cluster], a complete shorthand version of Eq. (26) takes shape. Equation (34) shows this form explicitly:

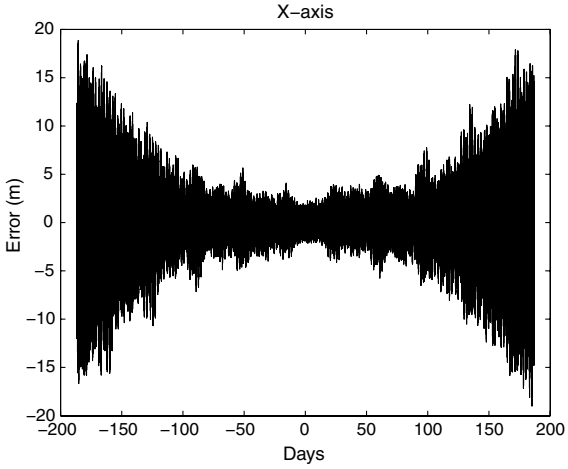

Fig. 6 Cluster decomposition torus fit, X axis ($a = 1.1\,R_{\oplus}$, $e = 0.05$, and $i = 30$ deg).

$$\begin{bmatrix} \Re(\mathcal{K}_{[\Psi_1]_{wrt\Psi_1}}) & \cdots & \Re(\mathcal{K}_{[\Psi_1]_{wrt\Psi_n}}) \\ \Im(\mathcal{K}_{[\Psi_1]_{wrt\Psi_1}}) & \cdots & \Im(\mathcal{K}_{[\Psi_1]_{wrt\Psi_n}}) \\ \vdots & \vdots & \vdots \\ \Re(\mathcal{K}_{[\Psi_n]_{wrt\Psi_1}}) & \cdots & \Re(\mathcal{K}_{[\Psi_n]_{wrt\Psi_n}}) \\ \Im(\mathcal{K}_{[\Psi_n]_{wrt\Psi_1}}) & \cdots & \Im(\mathcal{K}_{[\Psi_n]_{wrt\Psi_n}}) \end{bmatrix} \begin{bmatrix} C_{\Psi_1} \\ S_{\Psi_1} \\ \vdots \\ C_{\Psi_n} \\ S_{\Psi_n} \end{bmatrix} = \begin{bmatrix} \Re(\Phi(\Psi_1)) \\ \Im(\Phi(\Psi_1)) \\ \vdots \\ \Re(\Phi(\Psi_n)) \\ \Im(\Phi(\Psi_n)) \end{bmatrix} \tag{34}$$

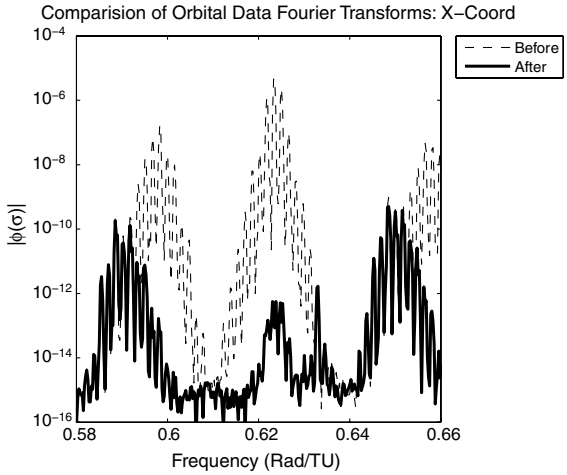

Fig. 7 Comparison of pre- and postdecomposition transforms.

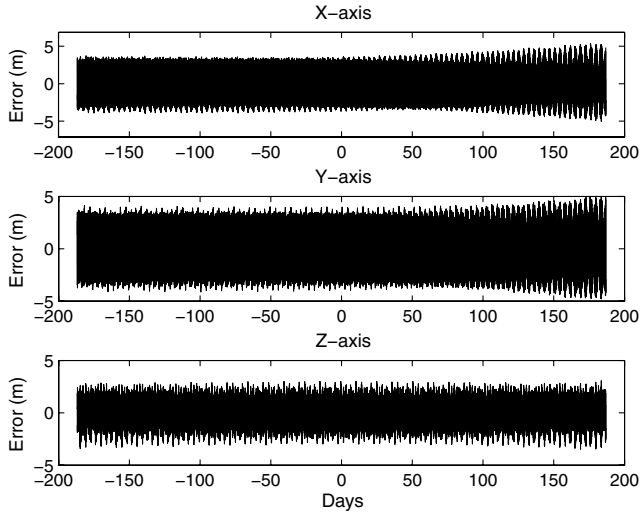

Fig. 8 HST orbital torus fit [$p = 2/\mathbf{M} = (6, 14, 6)$].

Table 2 Basis frequency set for the HST

Basis frequency	Value, rad/TU
Ω_1	0.880626013433404
Ω_2	0.059897412917959
Ω_3	0.001731861820452

Once the cluster coefficients have been solved for, the cluster is extracted from the data according to the following decomposition expression:

$$\mathbf{f}\,(t)_{k+1} = \mathbf{f}(t)_k - C_{\omega_k}\cos(\omega_k t) - S_{\omega_k}\sin(\omega_k t) \tag{35}$$

where k is the current iteration in the decomposition process and ω_k is the frequency corresponding to the k_{th} peak in transform, $\Phi(\omega)$, of the frequency cluster. As alluded to previously, the clusters should be processed in order of magnitude, largest to smallest, as to minimize effects from neighboring clusters' shoulders. This process should be repeated until desired accuracy in the fit is achieved.

VI. Numerical Results

A. Illustrative Example

As an illustrative example, the yearlong orbit depicted in Fig. 2 was decomposed and reconstructed using this frequency-cluster decomposition method with an $\mathbf{M} = (6, 14, 6)$ expansion of the basis set, where each element of $\mathbf{M}$ indicates the number of multiples of each basis frequency used. After decomposition, the orbit was recreated from the estimated basis set and numerically calculated Fourier coefficients. The residuals in the fit for the X axis can be found in Fig. 6. Residuals in the other axes have a similar character, which is expected due to the similarities seen between the axes in Fig. 2. The only significant difference was the maximum magnitude of the error seen in the Z axis; it was about half that of the X and Y axes. Since that axis has smaller coordinate values in the rotating frame, its residuals are naturally smaller. Regardless, the fit is clearly excellent, especially considering the time span is one year. The one-dimensional root-mean-square (rms) values for the X-, Y-, and Z-axis residuals are 3.87, 3.88, and 1.98 m, respectively. The maximum residuals in each axis were 18.83, 17.58, and 9.35 m, in the same order as previously listed.

Figure 7 shows a comparison of Fourier transforms before and after decomposition for a small portion of the X-coordinate axis. Note how the cluster peaks are cleanly removed from orbital data based on the index chosen for the third basis frequency. In this case, the value chosen was 6 and as such, one harmonic of Ω_3 was left in the central cluster. This peak roughly contributes error on the order of centimeters or less, but it could be removed with a simple increase of 1 in the third element of $\mathbf{M}$. The remaining clusters in this plot could be removed by increasing the second element of $\mathbf{M}$, as the centers of each cluster represent echoes of the second basis frequency, or by possibly fitting the binary cluster structure born from the collision of the two clusters. The latter would need to be done only if treating each cluster independently did not lead to clean decompositions of both cluster structures.

B. Orbit Prediction Example with Geopotential Only

For the decomposition of orbital tori concept to be useful, its effectiveness in predicting future ephemerides must be assessed. Of course, the basic assumption of this research is that Earth orbital tori are invariant, or at least nearly invariant on operational timescales.

Table 3 Summary of HST orbital torus fit

Basis set, rad/TU	Max error, m	1-D rms error, m
$\Omega_1 = 0.880626013433404$	$X = 5.36$	$X = 1.77$
$\Omega_2 = 0.059897412917959$	$Y = 4.99$	$Y = 1.78$
$\Omega_3 = 0.001731861820452$	$Z = 3.07$	$Z = 0.99$

[a] $a = 1.09\,R_{\oplus}$, $e = 0.0$, and $i = 28.5$ deg.

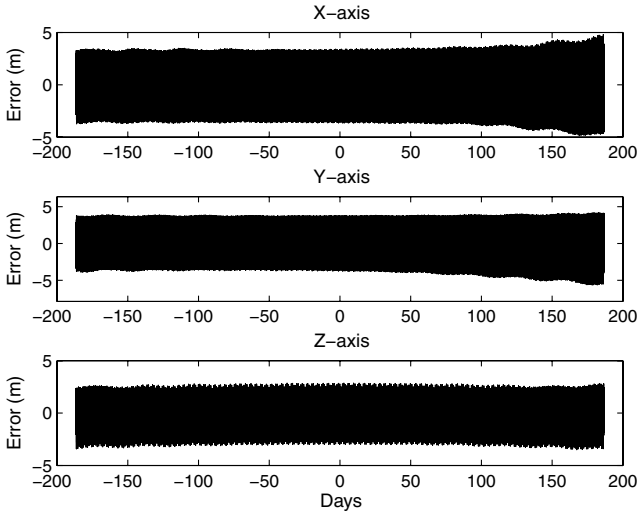

Fig. 9 HST orbital torus one-year prediction fit [M = (6, 14, 6)].

Thus, using a constructed orbital torus to estimate future orbital trajectories should produce error on the order of that encountered during the initial fitting process. If not, the assumption of invariance is poor and the orbital tori concept would be in jeopardy. To test the future validity of an orbital torus estimate, a sample orbit determination problem of real-world significance was undertaken. In particular, the Hubble Space Telescope (HST) was analyzed.

A NORAD two-line element set from 18 February 2010 was used as the reference orbit. As with the preceding analysis, the initial conditions were used within a Hamming numerical integrator to create a one-year sample of orbital position data. The time step within the data was 0.05 TU (time units), or approximately 40 s. Only the Earth's geopotential was used as a source of perturbations. Table 2 shows the basis set that was converged upon. Using this basis set, the frequency-cluster decomposition routine was applied on the data set using an $\mathbf{M} = (6, 14, 6)$ expansion to construct an initial torus estimate. The results can be seen in Fig. 8, with specific numerical results in Table 3. The fit is tight, with 1-D rms values of less than 2 m in each coordinate axis.

The future applicability of the torus estimate was tested on a one-year, integrated data sample created by the same integrator used previously, also using an $\mathbf{M} = (6, 14, 6)$ expansion. Chronologically speaking, this simulated orbital data was chosen such that it immediately followed the original data used to fit the orbital torus. The results can be seen in Fig. 9. Table 4 shows associated results in tabular form. The fit once again is very tight.

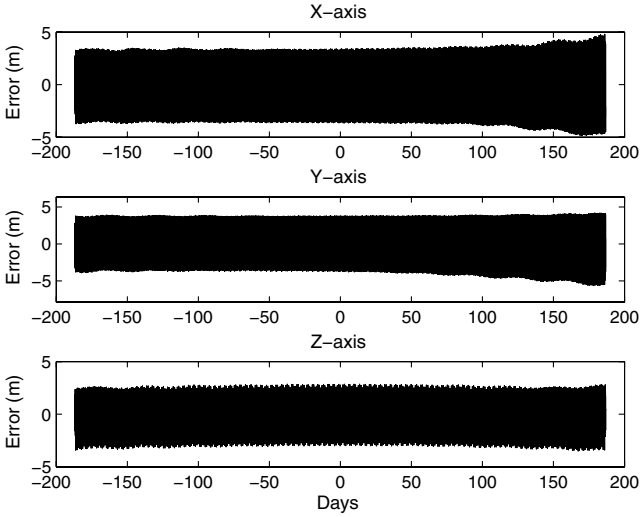

Fig. 10 HST orbital torus one-year prediction fit [M = (6, 20, 6)].

Table 4 Summary of HST orbital predication results[a]

Basis set, rad/TU	Max error, m	1-D rms error, m
$\Omega_1 = 0.880626013433404$	$X = 5.75$	$X = 1.82$
$\Omega_2 = 0.059897412917959$	$Y = 5.44$	$Y = 1.83$
$\Omega_3 = 0.001731861820452$	$Z = 3.16$	$Z = 0.99$

[a]$\mathbf{M} = (6, 14, 6)$, $a = 1.09\,R_\oplus$, $e = 0.0$, and $i = 28.5$ deg.

These results clearly support the assertion that at a minimum, a nearly invariant torus is the resulting motion of a satellite under the influence of the Earth's geopotential. The difference between the error from the original torus fit from the numerical data and the error from the torus fit from the predicted ephemeris is on the order of centimeters in each axis. In addition to numerical error, this small difference can be attributed to using a small sample of the torus to estimate the initial basis set and Fourier coefficients. Although the time sample of the orbit was chosen such that each frequency in the basis set had 10 or more revolutions, the motion on the torus is multiply periodic. As such, it never truly repeats due to the incommensurate nature of the basis set. Thus, it should be expected that different torus samples may create slightly different estimates of the basis set and Fourier coefficients. In an operational scenario, the use of a sequential estimation method at this point would make sense, thus allowing the parameters of the orbital torus to be refined over time.

Figure 10 shows the results from a $\mathbf{M} = (6, 20, 6)$ and demonstrates that time and computational power seem to be the only practical limits on how low the error can be reduced, as the error in the fit has been reduced by nearly a factor of 2 in each coordinate axis. However, at very large expansions in $\mathbf{M}$, the reduction in error is predominantly due to squeezing out ever-decreasing contributions from the signal that are not necessarily attributable to an underlying toroidal object. Although the fit will continue to marginally progress, the improvement is done so at unproportionate and unnecessary cost.

VII. Conclusions

This paper demonstrates a new frequency-cluster-based spectral decomposition method for orbital tori about the Earth. Rather than decompose one spectral line at a time, bands of lines (or frequency clusters) are decomposed from the orbital data by using the windowed form of the analytical, truncated, continuous Fourier transform (ATCFT), thus allowing the algorithm to compensate for local transform effects more precisely and efficiently. A Hanning window of order 2 was used to obtain torus fits with error as low as a few meters per coordinate axis in a years' worth of integrated LEO-type orbital position data. With clean, integrated data, the lower bound of error appears to be limited to the order of the expansion of the basis set as well as the length of the data vector used. The single-meter-per-axis error results were achieved with orbits containing 10 or more revolutions of the smallest nonnegligible orbital frequency in the data sampled. In related research, it has been shown that with fewer than 10 periods present, torus estimate error grows rapidly. At one period, error was in the thousands of meters and even as high as hundreds of thousands of meters, depending on the orbital parameters of semimajor axis, inclination and eccentricity chosen. Thus, although the decomposition of the spectra by frequency clusters presents itself as the way to construct an orbital torus, the Nyquist–Shannon theoremlike constraint limits the region of applicability, assuming relatively short tracks of data. As the time span of the data increases, so does the applicability of the method.

The results obtained also show that Kolmogorov–Arnold–Moser (KAM) tori appear to be a good way to compress ephemerides. For nonoperational or nonmaneuvering missions, where years of data can be obtained, trajectory-following methods may suffice for orbit determination. However, operational missions may have to wait for equations-of-motion-based methods. These methods would employ a direct map from the equations of motion themselves to the torus, as opposed to the indirect method of surveying years of orbital data.

References

[1] Kolmogorov, A. N., "The Conservation of Conditionally Periodic Motions with a Small Variation in the Hamiltonian," *Doklady Akademii Nauk SSSR*, Vol. 98, 1954, pp. 527–530.

[2] Moser, J., "On Invariant Curves of Area Preserving Mappings of an Annulus," *Nachrichten der Akademie der Wissenschaften in Gottingen II, Mathematisch-Physikalische Klasse*, Vol. 2, 1962, pp. 1–20.

[3] Arnold, V. I., "Proof of a Theorem of A. N. Kolmogorov on the Invariance of Quasi-Periodic Motions Under Small Perturbations of the Hamiltonian," *Russian Mathematical Surveys*, Vol. 18, No. 5, 1963, pp. 9–36.
doi:10.1070/RM1963v018n05ABEH004130

[4] Wiesel, W. E., "Earth Satellite Orbits as KAM Tori," *Journal of the Astronautical Sciences*, Vol. 56, April–June 2008, pp. 151–162.

[5] Binney, J., and Spergel, D., "Spectral Stellar Dynamics," *Monthly Notices of the Royal Astronomical Society*, Vol. 252, 1982, pp. 308–321.

[6] Binney, J., and Spergel, D., "Spectral Stellar Dynamics II—The Action Integrals," *Monthly Notices of the Royal Astronomical Society*, Vol. 206, 1984, pp. 159–177.

[7] McGill, C., and Binney, J., "Torus Construction in General Gravitational Potentials," *Monthly Notices of the Royal Astronomical Society*, Vol. 244, 1990, pp. 634–645.

[8] Binney, J., and Kumar, S., "Angle Variables for Numerically Fitted Orbital Tori," *Monthly Notices of the Royal Astronomical Society*, Vol. 261, 1993, pp. 584–592.

[9] Laskar, J., "Introduction to Frequency Map Analysis," *Hamiltonian Systems with Three or More Degrees of Freedom*, edited by C. Simo, Kluwer Academic, Boston, 1999, pp. 134–150.

[10] Laskar, J., "Frequency Map Analysis and Quasiperiodic Decompositions," *Proceedings of the Porquerolles School*, Sept. 2001, http://arxiv.org/abs/math/0305364v3 [retrieved Nov. 2010].

[11] Craft, C., "Formation Flight of Earth Satellites on KAM Tori," M.S. Thesis, Dept. of Aeronautics and Astronautics, Air Force Inst. of Technology, Dayton, OH, 2009.

[12] Little, B., "Application of KAM Theorem to Earth Orbiting Satellites," M.S. Thesis, Dept. of Aeronautics and Astronautics, Air Force Inst. of Technology, Dayton, OH, 2009.

[13] Arnold, V. I., *Mathematical Methods of Classical Mechanics*, 2nd ed., Springer, New York, 1989, Chaps. 5, 6, Appendix 5.

[14] Ott, E., *Chaos in Dynamical Systems*, 2nd ed., Cambridge Univ. Press, Cambridge, England, U.K., 2002, Chaps. 6, 7.

[15] Celletti, A., and Chierchia, L., "KAM Tori for *N*-Body Problems: A Brief History," *Celestial Mechanics and Dynamical Astronomy*, Vol. 95, 2006, pp. 117–139.
doi:10.1007/s10569-005-6215-x

[16] Delshams, A., and Gutiérrez, P., "Effective Stability and KAM Theory," *Journal of Differential Equations*, Vol. 128, No. 2, 1996, pp. 415–490.
doi:10.1006/jdeq.1996.0102

[17] Nekhoroshev, N. N., "An Exponential Estimate of the Time of Stability of Nearly-Integrable Hamiltonian Systems," *Russian Mathematical Surveys*, Vol. 32, No. 6, 1977, pp. 1–65.
doi:10.1070/RM1977v032n06ABEH003859

[18] Vallado, D. A., *Fundamentals of Astrodynamics and Applications*, 3rd ed., Microcosm, Hawthorne, CA, 2007, Chaps. 8, 9.

[19] Wodnar, K., "A New Fast Fourier Method for Evaluating Fourier Spectra at Arbitrary Frequencies," *Celestial Mechanics and Dynamical Astronomy*, Vol. 65, Nos. 1–2, 1997, pp. 85–94.
doi:10.1007/BF00048440

[20] Gomez, G., Mondelo, J. M., and Simoó, C., "A Collocation Method for the Numerical Fourier Analysis of Quasi-Periodic Functions. I: Numerical Tests and Examples," *Discrete and Continuous Dynamical Systems. Series B*, Vol. 14, No. 1, 2010, pp. 41–74.
doi:10.3934/dcdsb.2010.14.41

[21] Wiesel, W. E., *Modern Astrodynamics*, Aphelion Press, Beavercreek, OH, 2003, Chap. 4.